An Objective Detection Method for Convective Cold Pool Events and Its Application to Northern Africa

ROBERT REDL

Institute for Geophysics and Meteorology, University of Cologne, Cologne, Germany

ANDREAS H. FINK AND PETER KNIPPERTZ

Institute of Meteorology and Climate Research, Karlsruhe Institute of Technology, Karlsruhe, Germany

ABSTRACT

Convective cold pool events in (semi) arid areas have significant impacts on their environment. They reach horizontal extents of up to several hundred kilometers and the associated turbulence and shear can cause dust emissions and threaten aviation safety. Furthermore, cold pools play a major role in the organization of deep convection and in horizontal moisture transport. They have even been proposed to have impacts on larger-scale monsoon dynamics. Cold pools are not well represented in models using a convective parameterization. To test and improve these models, it is necessary to reliably detect cold pool occurrence from standard observational data. Former studies, however, focused on single cases or short time periods.

Here, an objective and automated method for the generation of multiyear climatologies of cold-pool events is presented. The algorithm combines standard surface observations with satellite microwave data. Representativeness of stations and influence of their spatial density are addressed by comparison to a satellite-only climatology. Applying this algorithm to data from automatic weather stations and manned synoptic stations in and south of the Atlas Mountains in Morocco and Algeria reveals the frequent occurrence of cold pool events in this region. On the order of six cold-pool events per month are detected from May to September when the Saharan heat low is in its northernmost position. The events tend to cluster into several-days-long convectively active periods, often with strong events on consecutive days. The algorithm is flexible enough to be applied in comparable regions around the world.

1. Introduction

The cold air formed by evaporation and melting of precipitation below a convective cloud system behaves like a density current (e.g., Simpson 1987; Weisman and Rotunno 2004). It descends to the ground and spreads out horizontally driven by the density difference to the warmer surrounding air. Cold pools created in this way are an inherent part of many convective systems, but typically the largest dimensions of this feature are observed in low-latitude arid or semiarid regions. There, optimal conditions for the evaporation are provided by a deep, warm, and dry daytime convective boundary layer. A further enhancement of the evaporative cooling

typically happens when vertical wind shear separates up- and downdrafts (Coniglio et al. 2006; Cohen et al. 2007; Roberts and Knippertz 2014). A horizontal extent of hundreds of kilometers and a depth of up to 3 km are not unusual and are often reached by merging of several smaller cold pools (Knippertz et al. 2009a). The highly turbulent gust fronts of cold pools can lead to significant dust emissions, which are then called haboobs. Their occurrence is documented for many dry regions around the planet. Sutton (1925) and Farquharson (1937) were among the first to describe the occurrence and characteristics of haboobs in the Sahelian part of the eastern African country of Sudan; more recent literature addressed the Sahel (e.g., Marsham et al. 2008; Williams 2008; Knippertz and Todd 2010; Marsham et al. 2013b), northwest Africa (e.g., Knippertz et al. 2007; Emmel et al. 2010), the Middle East (e.g., Offer and Goossens 2001; Miller et al. 2008), the Gobi Desert in China (Takemi 2005), Australia (Strong et al. 2011), the

Corresponding author address: Robert Redl, Institute for Geophysics and Meteorology, University of Cologne, Pohligstr. 3, 50969 Cologne, Germany.
E-mail: rredl@meteo.uni-koeln.de

Chihuahuan Desert between the United States and Mexico (Rivera Rivera et al. 2010), and the Great Plains of the United States (Chen and Fryrear 2002). Many of these regions are uninhabited and events remain unrecognized, but from time to time haboobs gain public attention when larger cities like Phoenix, Arizona, are hit (e.g., Raman et al. 2014).

These large cold pool events have several important effects on their environment. Observational and modeling studies (Marsham et al. 2013b; Heinold et al. 2013) show that up to half of the mineral dust emissions in the Sahel and southern Sahara during the summer are caused by cold pools. Even without substantial dust emissions, cold pools are a serious threat for aviation as a result of rapid changes in wind shear between downdrafts of up to $10\,\mathrm{m\,s^{-1}}$ that feed the systems combined with updrafts of up to $6\,\mathrm{m\,s^{-1}}$ at the turbulent head (Goff 1976; Linden and Simpson 1985). The updrafts are created by the lifting of warm air above the head of the density current, a process that can lead to arc cloud formation and that is also involved in storm propagation by the triggering of new convective cells (Goff 1976). Indeed, cold pools are a key factor for the organization of single cells into larger mesoscale convective systems (MCSs) and their movement, as pointed out by Zipser (1977) and later confirmed by many others (e.g., Corfidi 2003; Weisman and Rotunno 2004). Recently, large-scale effects of cold pools from Sahelian squall lines on the West African monsoon (WAM) system have been highlighted by Marsham et al. (2013a). This study also shows that cold pools form a significant part of the low-level northward moisture flux in the WAM and of the ventilation of the Saharan heat low.

The fundamental physics behind cold pool generation by density currents are well understood and were discussed in detail decades ago (e.g., Simpson 1987). However, today's climate models still show significant uncertainties for projected changes in the WAM (Xue et al. 2010; Druyan 2011) and other monsoon regions (Christensen et al. 2013) regularly affected by convective cold pools. One major reason known is that these models are unable to create realistic cold pools is the usage of parameterizations of deep convection (Heinold et al. 2013; Marsham et al. 2013a). Related effects such as dust emissions and modification of the monsoon flow can then further contribute to uncertainties and model error. For example, the models used for the Fifth Assessment Report of the Intergovernmental Panel on Climate Change all tend to underestimate dust emissions over northwest Africa (Evan et al. 2014).

Given the role of convectively generated cold pools for monsoonal heat low ventilation and moistening, dust emissions, and severe convective storm generation, there is a clear need for automated algorithms to create multiyear climatologies of cold pool occurrences. So far, only a few studies on climatological aspects exist. The first historical report from Sudan contained an 8-yr climatology of haboobs for Khartoum, Sudan [24.5 cases per year; Sutton (1925)]; Engerer et al. (2008) analyzed 8 yr (only April–August) of station and radar data from Oklahoma; and Emmel et al. (2010) identified cold pools over the northwest African Atlas Mountains based on a subjective and labor-intensive manual inspection of station data and infrared satellite images.

The purpose of this paper is the presentation of a new objective method suitable for creating multiyear climatologies of cold pool events based on station observations of standard meteorological variables combined with microwave satellite data. The algorithm is objective in the sense that individual case decisions are based on fixed thresholds and thus are reproducible. Though the thresholds have been selected for an application to northern Africa, they can be adapted to fit to others regions. The algorithm depends on freely available data and is therefore applicable to all relevant regions worldwide. The method is based on Emmel et al. (2010), but extends their work. Thus, results are presented for northwest Africa including the Atlas Mountains and large parts of the western Sahara Desert.

Section 2 gives an overview of the station and satellite data used in this paper. The actual cold pool detection method is described in section 3. The resultant climatology for northwest Africa is discussed in section 4 and concluding remarks are given in section 5.

2. Data

The new algorithm presented here needs surface observations, namely dewpoint temperature, wind speed and direction, and precipitation, as well as satellite observations of brightness temperatures at microwave frequencies. Surface observations are used to detect typical characteristics of the leading edge of a cold pool, followed by the detection of at least one nearby convective system in satellite observations to support the passage of a cold pool at the station. Two sources of surface observations are used and their feasibilities for the purpose of detecting cold pool events are compared. These two sources are automatic weather stations (AWSs) with high temporal resolution and standard reports from synoptic stations and airports.

a. IMPETUS station network

The main focus of this paper is on northwest Africa, a generally data-sparse region that is regularly affected
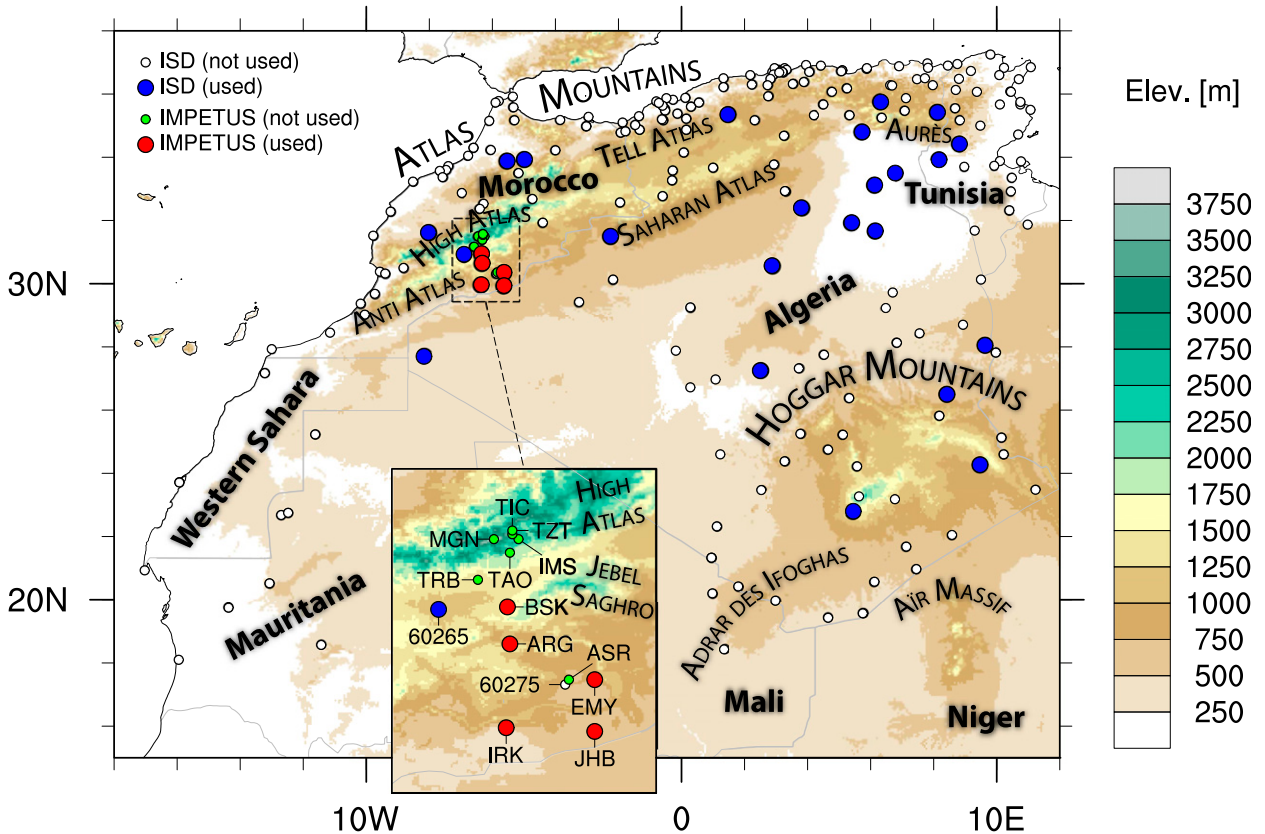
FIG. 1. Geographical overview of northwest Africa including locations of ISD and IMPETUS weather stations.

by convective cold pool events, especially along the southern flank of the Atlas Mountains, as shown by Emmel et al. (2010). This study provides a climatology for five years (2002–06) and serves as a reference for the new algorithm when applied to this region, which makes the selected area an interesting test case. Like Emmel et al. (2010), the current study benefits from a dense network of AWSs deployed by the An Integrated Approach to the Efficient Management of Scarce Water Resources in West Africa (IMPETUS) project (Speth et al. 2010) in southern Morocco. The AWSs were equipped with instruments for air temperature and humidity, soil temperature and humidity, global and net radiation, wind speed and direction, and precipitation. Data from 11 stations are available from 2002 until 2012. They are located in the basins of the rivers Dadès and Drâa and cover parts of the M'Goun mountain massif in the High Atlas and the Jebel Saghro mountain range that belongs to the Anti Atlas mountain range (Fig. 1; Table 1). The year 2012 is only available until the second half of September, when the stations were dismantled. Five stations have been selected here for the climatology because of their location south of the High Atlas and their data

availability. These stations are Bou Skour (BSK), Arguioun (ARG), El Miyit (EMY), Jebel Brâhim (JHB), and Lac Iriki (IRK) (red markers in Fig. 1). The average distance from one station to its closest neighbor is 46 km. The measurement intervals of these stations differ between 10 and 15 min. For the sake of easier processing, all measurements were interpolated linearly to 5-min intervals.

TABLE 1. Locations of IMPETUS stations and data availability for the period 2002–12.

Station	Abbreviation	Lat (°N)	Lon (°W)	Elev (m)	Availability (%)
Arguioun	ARG	30.65	6.32	1020	70.1
Bou Skour	BSK	30.95	6.34	1420	98.5
El Miyit	EMY	30.36	5.63	792	95.5
Imeskar	IMS	31.50	6.25	2245	86.0
Lac Iriki	IRK	29.97	6.35	445	93.1
Jebel Brâhim	JHB	29.94	5.63	725	58.4
M'Goun	MGN	31.50	6.45	3850	94.8
Taoujgalt	TAO	31.39	6.32	1900	79.9
Tichki	TIC	31.54	6.30	3260	79.1
Trab Labied	TRB	31.17	6.58	1383	91.0
Tizi-n-Tounza	TZT	31.57	6.30	2960	53.4

b. SYNOP and METAR

Standard surface synoptic observations (SYNOPs, format FM-12) and aviation routine weather reports (METARs, format FM-15), both described in WMO (2010), are a valuable source of information and are available worldwide. However, the station density in northwest Africa is relatively low compared to other regions of the world. Here, we do not use raw reports but the quality controlled Integrated Surface Database (ISD; Smith et al. 2011) compiled by the National Climatic Data Center (NCDC). This dataset mainly consists of hourly reports, but also has a number of half-hourly observations. For the entire region of interest (Fig. 1), 224 stations are available. Because of their reporting frequency, not all of these stations are suitable for the creation of a climatology. Only those stations with a data availability of more than 80% with respect to hourly observations for the period 2002–14 have been selected. Also, stations with a distance of less than 100 km from the coastline have been removed to avoid detection of sea-breeze fronts, which are technically also density currents and can have characteristics very similar to convectively driven cold pools. The remaining dataset contains 23 stations (blue markers in Fig. 1) with an average distance from one station to its closest neighbor of 184 km. Like the AWS data, these observations were also interpolated linearly to 5-min intervals.

c. AMSU-B and MHS microwave data

Infrared satellite images from the Meteosat Spinning Enhanced Visible and Infrared Imager (SEVIRI) have been used in a number of studies that investigated cold pool events and dust emissions in west and northwest Africa (e.g., Marsham et al. 2013b; Allen et al. 2013; Bou Karam et al. 2014). In these studies the "desert dust" product (Lensky and Rosenfeld 2008), which is a red–green–blue (RGB) composite of three infrared channels, was used. The advantage of this product is its high spatiotemporal resolution (15 min, 0.03°) combined with its ability to show the leading edge of the cold pool by means of emitted dust. While this is useful for case studies of single events, two other aspects of this product become important for the creation of a climatology. First, dust is only visible in the absence of high-level clouds and it is hard to distinguish between deep convective clouds that can generate a cold pool and other high-level clouds that cannot. Since cold pools originate from deep convection, which is usually surrounded by extensive high-level cirrus shields, it is to be expected that events are missed when relying on infrared images (Ashpole and Washington 2013; Kocha et al. 2013). This

is further supported by Heinold et al. (2013), who showed that up to 90% of cold-pool-related dust emissions in high-resolution model simulations are at least partly covered by clouds. Second, atmospheric column water vapor (CWV) can completely mask the dust signal (Brindley et al. 2012). Unfortunately, the CWV is increased by the presence of a cold pool.

To avoid these problems, the method discussed in this paper makes use of microwave satellite data, namely the Advanced Microwave Sounding Unit-B (AMSU-B) on board NOAA-15, -16, and -17 satellites, as well as the Microwave Humidity Sounder (MHS), which is the successor of AMSU-B on board NOAA-18 and -19 and MetOp-A and -B. All these satellites are polar orbiting. Both instruments have two windows channels, 89 and 150 GHz (AMSU-B) or 157 GHz (MHS), and three channels at the 183.3-GHz water vapor absorption line. For AMSU-B, these channels are 183.3 ± 1, ±3, and ±7 GHz, and for MHS 183 ± 7 GHz is replaced by 190 GHz. Both instruments are designed as cross-track line-scanned radiometers with an antenna beamwidth of 1.1°. Together with the nominal altitudes of 850 km (AMSU-B) and 870 km (MHS), this translates to nadir resolutions of 16.3 km (AMSU-B) and 17 km (MHS). The swath width for each is approximately 2200 km. These instruments are able to reliably detect deep convection (Burns et al. 1997; Bennartz and Bauer 2003; Hong 2005). An example from June 2011 illustrates the advantage of the microwave instruments: the infrared image (Fig. 2a, desert dust product) shows high-level clouds in a wide region over the Atlas Mountains, while in the microwave brightness temperature images (Figs. 2b–d) the cores of the convective systems are clearly visible. For the region of interest, 106 582 satellite overpasses (approximately 0.7 TB of data) were selected for the period 2002–14, which corresponds to 22 overpasses per day on average. However, the number of overpasses per year is not constant since the number of satellites has changed over time. The smallest number of overpasses is available for 2002 (11.3 overpasses per day), the largest number for 2013 (28.7 overpasses per day).

Data were obtained as raw instrument counts (level 1b) from the NOAA Comprehensive Large Array-Data Stewardship System (CLASS) and converted to brightness temperatures (level 1c) using the ATOVS and AVHRR preprocessing package (AAPP; Labrot et al. 2011). This conversion also includes a correction for radio frequency interference (RFI), which is especially crucial for NOAA-15 (Atkinson 2001).

Products using data from spaceborne radar instruments, like those aboard TRMM and GPM satellites, were not taken into account due to their lower spatiotemporal coverage. This lower coverage is caused
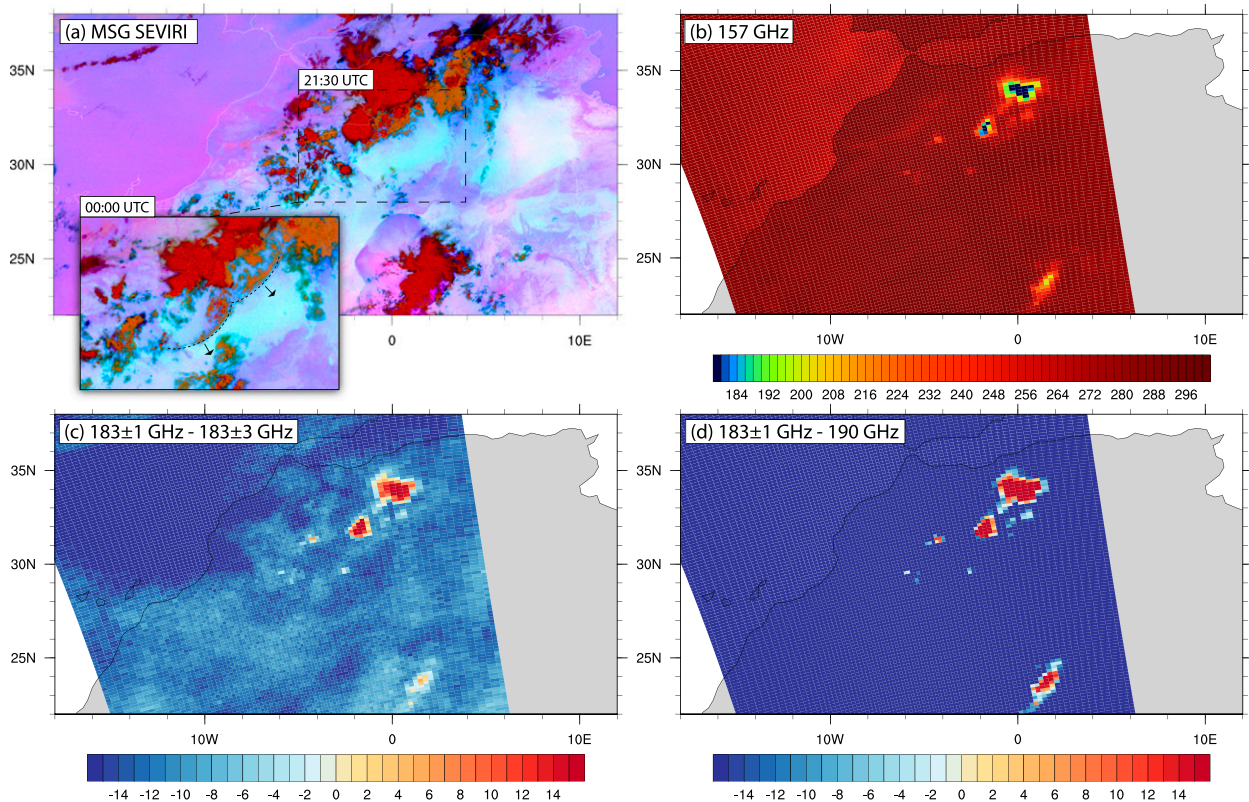
FIG. 2. Comparison of infrared and microwave data for a cold pool event on 21 Jun 2011: (a) Meteosat SEVIRI ''desert dust'' product at 2130 UTC (whole area) and 0000 UTC (elevated detail, dashed lines and arrows indicate leading edge of cold pool and direction of propagation, respectively). Data from *MetOp-B* overpass at 2121 UTC: (b) brightness temperature of the 157-GHz channel, (c) difference between brightness temperature of the 183 ± 1 and 183 ± 3 GHz channels, and (d) difference between brightness temperature of the 183 ± 1 and 190-GHz channels.

by the smaller number of satellites combined with smaller swath widths. Moreover, blended rainfall products derived from these and other satellites incorporate infrared measurements with the flaws mentioned above, rendering these gridded products inadequate for the task of convection screening.

3. Methods

a. The cold pool detection algorithm

The objective cold pool detection algorithm consists of three steps: (i) preselection of cases based on station data, (ii) grouping of contemporaneous cases from multiple stations into single events, and (iii) confirming the existence of a nearby convective system based on microwave satellite data.

In the first step, station data are screened for typical characteristics of the leading edge of a convectively generated cold pool. In general, these characteristics are high horizontal wind speeds, high turbulent kinetic energy (TKE), increases in surface pressure, decreases in temperature, and increases in dewpoint temperature

(e.g., Knippertz et al. 2007; Engerer et al. 2008). As in Emmel et al. (2010), only the most stable and with the selected data sources available indicators, which are mean horizontal wind speed v_{mean} and increase in dewpoint temperature ΔT_d, are ultimately used (an example case is shown in Fig. 3). The selected thresholds are $\Delta T_d \geq 4$ K in 30 min and $v_{mean} \geq 4$ m s^{-1} in the following hour. In addition to these thresholds, another requirement is there be no precipitation ±1 h around the detected jump in T_d, since rainfall near the station can increase T_d in the absence of a convective cold pool event. Ignoring stations that are directly affected by rain does not hinder the detection of large events, as they usually affect multiple stations. However, the absolute number of cases detected in the data from the IMPETUS stations is reduced by about 32% as a result of this criterion. The above-described thresholds are identical to those chosen in Emmel et al. (2010) and based on case studies of cold pool events south of the Atlas Mountains (Knippertz et al. 2007). In some rather rare instances, these thresholds are also exceeded by smaller events not of interest here, such that an additional threshold for the
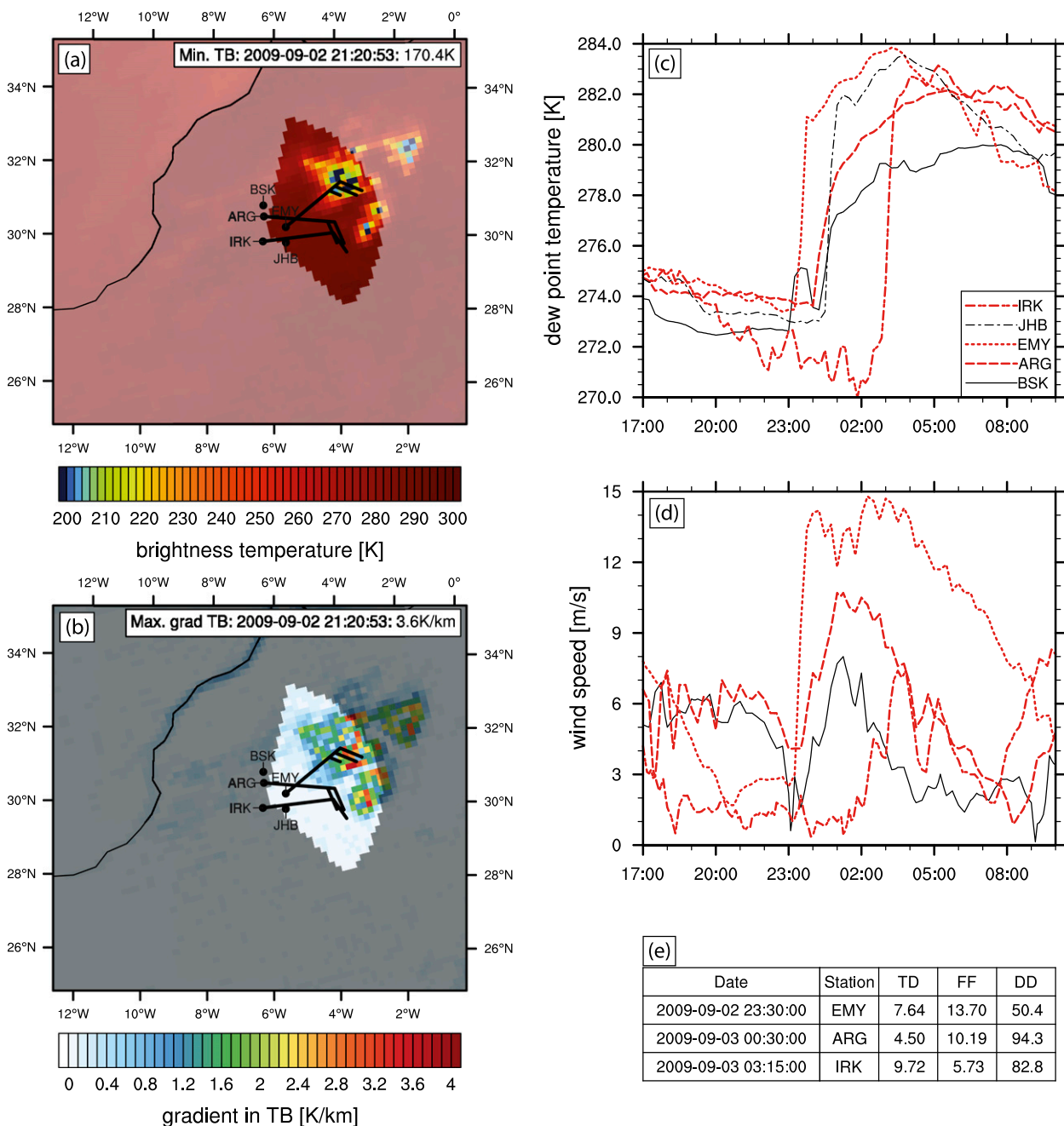
FIG. 3. An example case detected by the automated algorithm in ground observations from the IMPETUS station network (Fig. 1; Table 1) and satellite observations from *MetOp-B* in September 2009: (a) brightness temperatures measured in the 157-GHz channel; (b) horizontal gradient in brightness temperatures of the 157-GHz channel; (c) dewpoint temperature measured by AWS; and (d) wind speed measured by AWS, JHB is not included because of an instrument failure at the time. Red colors in (c) and (d) indicate fulfilled criteria. (e) Overview of measured values in tabular form (showing only stations that fulfill the criteria: TD = increase in dewpoint temperature, FF = mean wind speed in the hour following the dewpoint increase, and DD = mean wind direction in the hour following the dewpoint increase). The wedge-shaped brighter areas in (a) and (b) indicate the pixels used by the algorithm for convection screening.

dewpoint temperature was defined: the average of 1 h after the detected jump has to be 2 K larger than the average 1 h before the jump. The other indicators mentioned before suffer from different difficulties but could

potentially be used in the presence of appropriate measurement equipment to reduce uncertainties: turbulence is not reported from synoptic stations and not measured from the AWSs in use; the increase in surface pressure is

often weak and only detectable with high precision instruments; a decrease in temperature with the arrival of the cold pool can be masked at night by downward mixing of warmer air from above a surface inversion (Knippertz et al. 2007).

The thresholds described above are well suited for AWSs with a high measurement frequency, which in the case of the IMPETUS station network is 10–15 min. However, for an application to synoptic stations, longer measurement intervals need to be considered. This is neither for the precipitation and wind speed criteria, nor for the difference in T_d 1 h before and after the passage of concern. But the actual abrupt jump in T_d during the passage of a cold pool's leading edge is often not well captured. The best-case scenario for a measurement interval of 1 h is that the passage falls between two measurements. In this case a measured increase of 4 K would result in 2 K $(30\,\mathrm{min})^{-1}$. The worst-case scenario is that the passage coincides with one measurement. In this case half of the 4-K increase would happen before the measurement; the other half afterward. This would result in 4 K $(2\,\mathrm{h})^{-1}$ or 1 K $(30\,\mathrm{min})^{-1}$. This issue was addressed statistically by thinning out the observations from the IMPETUS station network to hourly temporal resolution. The threshold for ΔT_d was then reduced in 0.1-K steps until the minimal bias between the number of events detected with full and reduced temporal resolution was reached. Fortunately, the worst-case scenario mentioned before is much less likely and the actual increase in T_d is often significantly larger than 4 K. The minimal bias (+3.1%) was reached for $\Delta T_d = 2.5$ K, where 255 of 357 single-station events were matched, 113 events were added, and 102 events were removed. The procedure was repeated for a temporal resolution of 30 min, where the minimal bias (+3.4%) was reached with $\Delta T_d = 3.5$ K. In this case 308 of 357 events were matched, 61 events were added, and 49 events were removed.

The characteristics of the leading edge are very likely detected at multiple stations at the same time or within a short time period, especially in the case of a dense station network like the one described in section 2a. The number of stations where the detection thresholds are exceeded could provide information about the strength or spatial extent of the events, but should otherwise not influence the climatology. Thus, in the second step of the algorithm, cases detected at single stations that happen nearly simultaneously are grouped together into single events, as they belong very likely to the same cold pool or at least to the same convective episode, which can create several connected cold pools. Emmel et al. (2010) used fixed time intervals for all pairs of stations for this purpose. Here, in

order to make the algorithm applicable to other station networks as well, the maximum time difference between two station cases depends on the distance between the stations (Δx) and the average of the observed wind speed at both stations (v_1 and v_2). The selected criterion is that the propagation of the cold pool should not be slower than the half of the observed wind speed. This results in a maximum time difference for the detection at both stations of $\Delta t_{\max} = 4\Delta x/(v_1 + v_2)$. If the observed time difference is larger than $\Delta t_{\max}$, then the single cases are considered to have different sources. In addition to the time criterion, a maximum distance Δx of 1000 km is allowed. As in Emmel et al. (2010), an event is classified as a cold pool event if it is observed at least at two stations. Cases that are only detected at one station, but are too weak to exceed the thresholds at another one, are ignored for the climatology. This criterion has a quite restrictive effect as more than half of the cases detected in the IMPETUS network are only detected at one station. But its application together with the requirement for no rain ± 1 h and the persistently increased T_d for 1 h ensures that the created climatology is a conservative estimation for the occurrence of large-scale cold pool events and not biased by the potentially much more frequent occurrence of smaller-scale cold pools and microbursts.

Not only convective cold pool events are selected by the first two steps of the algorithm, but also large-scale flows like cold inflows from an adjacent ocean or synoptic cold fronts could fulfill the same criteria. These synoptic-scale features are better reproduced than cold pools by numerical models. Since model evaluation is an intended application of the created climatologies, the third step of the algorithm is designed to remove those events not related to deep convection by means of microwave satellite data. Satellite overpasses from a time window of -6 to $+3$ h around the event are selected. These overpasses are scanned for convection in a radius of 324 km (6 h $\times$ 15 m s^{-1}) around the involved stations in a view angle of $\pm 60°$ relative to the mean observed wind direction (an example for this wedge-shaped area is shown in Figs. 3a and 3b). The selected value of 15 m s^{-1} is the mean wind speed found by Engerer et al. (2008) for cases in Oklahoma. Here, this value was adopted, although Knippertz et al. (2007) found somewhat lower values of 8–12 m s^{-1}.

A summary of all applied criteria for the detection of convective cold pool events is given in Table 2.

b. Microwave satellite convection screening criteria and limb correction

In the microwave channels of AMSU-B and MHS convection becomes visible through a reduction of brightness temperatures as a result of scattering by large ice

TABLE 2. Criteria applied during the three steps of the convective cold pool event detection algorithm. Symbols used are T_d for dewpoint temperature in 2 m, t_{max} for maximal time difference between the detection at two stations, Δx for distance between two stations, v_i for wind speed measured at the ith station, and v_{mean} for mean wind speed in 60 min.

Description	Threshold
Step 1: Preselection of cases based on station data	
Increase of dewpoint temperature (ΔT_d) within 30 min	$\geq$2.5–4 K (observation interval dependent)
Difference between mean T_d within 60 min after jump in T_d and 60 min before jump in T_d	$\geq$2 K
Mean wind speed (v_{mean}) within 60 min after jump in T_d	$\geq$4 m s^{-1}
Precipitation $\pm$1 h around jump in T_d	0 mm
Step 2: Grouping of contemporaneous cases from multiple stations into single events	
Maximal time between jump in T_d at two stations	$\Delta t_{max} = 4\Delta x/(v_1 + v_2)$
Maximal distance between stations (Δx)	1000 km
Minimal number of stations for one event	2
Step 3: Confirming the existence of a nearby convective system based on microwave satellite data	
Convective event detected by gradient in 150/157-GHz brightness temperature	$\geq$1.8–2.55 K (scan position dependent)
Maximal distance between station(s) and convection in satellite imagery	324 km (6 h $\times$ 15 m s^{-1})
Maximal angle between wind direction and connection line between station(s) and convection in satellite image	60°

particles. Bennartz and Bauer (2003) found the 150-GHz window channel to be most sensitive to these particles, and concluded that this channel should be used in mid- and high latitudes. However, this channel is also sensitive to the surface emissivity, which in turn is affected by snow cover, a phenomenon not uncommon for the High Atlas mountain range in winter and spring. An alternative, which is not sensitive to surface emissivity, is to use the channels around the water vapor absorption line at 183.3 GHz, since their weighting functions peak above 10 km. Burns et al. (1997) suggested to use the difference between the 183.3 $\pm$ 1 and $\pm$3 GHz channels for convection screening. This approach is only well suited for the tropics, because of the high-altitude peak in the weighting function of these channels (Bennartz and Bauer 2003). Hong (2005) used all three channels around 183.3 GHz as a method for detecting convection and convective overshooting between 30°S and 30°N. His criterion is that the difference between 183.3 $\pm$ 1 and $\pm$3 GHz as well as the difference between 183.3 $\pm$ 1 and $\pm$7 GHz is positive (at nadir).

The differences between the 183-GHz channels draw a very clear distinction between areas with active convection and their surroundings (cf. Figs. 2c and 2d). Unfortunately, these channels are affected by noise in many instances. On the one hand, this is due to RFI as mentioned in section 2c, and on the other hand, an increase in noise levels over time was found within the 183-GHz channels of some satellites. A simple, but effective algorithm for estimating the noise variance of

images, originally designed for the processing of photographs (Immerkær 1996), was applied to detect affected overpasses. It turned out that the *NOAA-15*, *-16*, and *-19* satellites were particularly affected by increasing noise levels. To obtain a method of convection screening that is stable over time, it was therefore decided to use the 150- or 157-GHz channel, which is unaffected by noise. To overcome the surface emissivity issue, the horizontal gradient of the brightness temperatures was used rather than the values themselves. In addition, pixels with a distance of less than 50 km to the coastline were ignored. For the gradient, a threshold of 2.55 K was chosen by comparing the 150/157-GHz and 183-GHz channels for all noise-free satellite overpasses. At nadir, this yields the same number of cases as does the Hong (2005) algorithm. Cases are defined here as one pixel or a contiguous block of several pixels above the threshold.

Like other cross-track scanning instruments, AMSU and MHS are affected by a so-called limb effect. This effect arises from the shorter path through the atmosphere at nadir compared to the outer scan positions. Thus, the weighting functions at outer scan positions are shifted upward in altitude (Goldberg et al. 2001) and render constant thresholds for the detection of convection problematic. This issue can be addressed by a correction of the brightness temperatures themselves (cf. Wark et al. 1993; Goldberg et al. 2001; Eymard et al. 2010) or, alternatively, by scan-position-dependent thresholds (cf. Hong 2005). We opted for the latter,
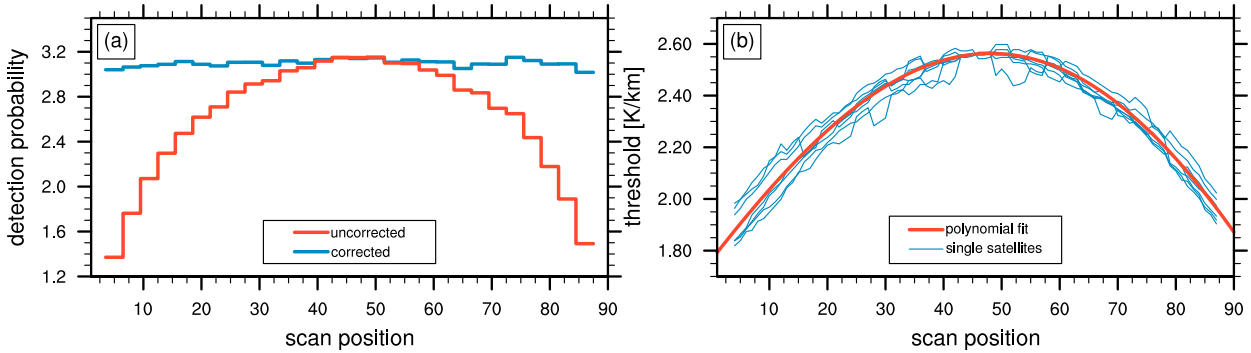
FIG. 4. (a) Probability to detect for a convective event (number of events per 10 000 pixel), binned every three pixels across the track before and after limb-effect correction. (b) Threshold for brightness temperature gradients in the 150/157-GHz channel for convection screening after limb-effect correction.

since we are not interested in absolute brightness temperature values.

Based on a cloud model and a radiative transfer model, Hong (2005) suggested a threshold between 0 K at nadir and about 20 K at the outermost scan positions for the differences of the 183.3-GHz channels. In a more recent review of the Hong algorithm based on observations, a much smaller view-angle dependency of 3.2–5.0 K was found (Xu et al. 2009). These authors considered this to be negligible and suggested a constant threshold of 0 K. Even if hardly visible by eye (see Fig. 2b), the 150/157-GHz channel is significantly affected by the limb effect. The outermost scan positions appear darker. To quantify this effect for the gradient-based convection screening, the probability of detecting an event was calculated for three-pixel-wide bins that were aligned in an across-track direction. The outermost bins were ignored, as the edge of the swath often cuts through a convective system. Without a limb effect, it should be equally probable to detect an event for each scan position. However, it was found that it is more than twice as likely to detect convection in the center of the swath compared to the margins (Fig. 4a).

A prerequisite for a meaningful climatology is to overcome this view-angle dependency for the convection screening. Therefore, a correction procedure was developed with the aim of getting at each scan position the same detection probability as at nadir. We use an iterative procedure with three steps in which only land pixels are considered: 1) calculation of the detection probability for convective events (p_{conv}) and calculation of the empirical complementary cumulative density function (CCDF = 1 − CDF) of the gradient in brightness temperature (CCDF$_{grad}$) for each scan position x; 2) calculation of the ratio between the detection probability at nadir and at each scan position x,

$$r[x] = p_{conv}[\text{nadir}]/p_{conv}[x], \qquad (1)$$

where the nadir value of p_{conv} is the average over the two central three-pixel bins; and 3) selection of a new threshold ($T_{new}[x]$) for each scan position with a probability of occurrence $r[x]$ times higher than the original one,

$$q_{new}[x] = \text{CCDF}_{grad}(T_{old}[x]) \times r[x] \quad \text{and} \qquad (2)$$

$$T_{new}[x] = \text{CCDF}_{grad}^{-1}(q_{new}[x]). \qquad (3)$$

Finally, a fourth-order polynomial is fitted to the new thresholds.

The event detection probability is not directly proportional to probabilities of gradient values at individual pixels. The reason is that an event consists of several continuous pixels above the threshold and the number of pixels per event also depends on the scan position. Thus, applying Eqs. (1)–(3) does not directly yield the result shown in Fig. 4 but is only a step in this direction. After six iterations, this procedure results in an almost flat detection characteristic. It is worth noting that the final thresholds (Fig. 4b) are not symmetric about the center. This can be explained by asymmetries in the measured brightness temperatures themselves. These asymmetries actually differ from satellite to satellite (Buehler et al. 2005b), but this was ignored here as the number of overpasses per satellite would otherwise not have been sufficient for a robust statistic.

4. Results

a. Climatology with station data

The convective cold pool detection algorithm was first applied to the IMPETUS station network described in section 2a. The year-to-year variability within the 10-yr
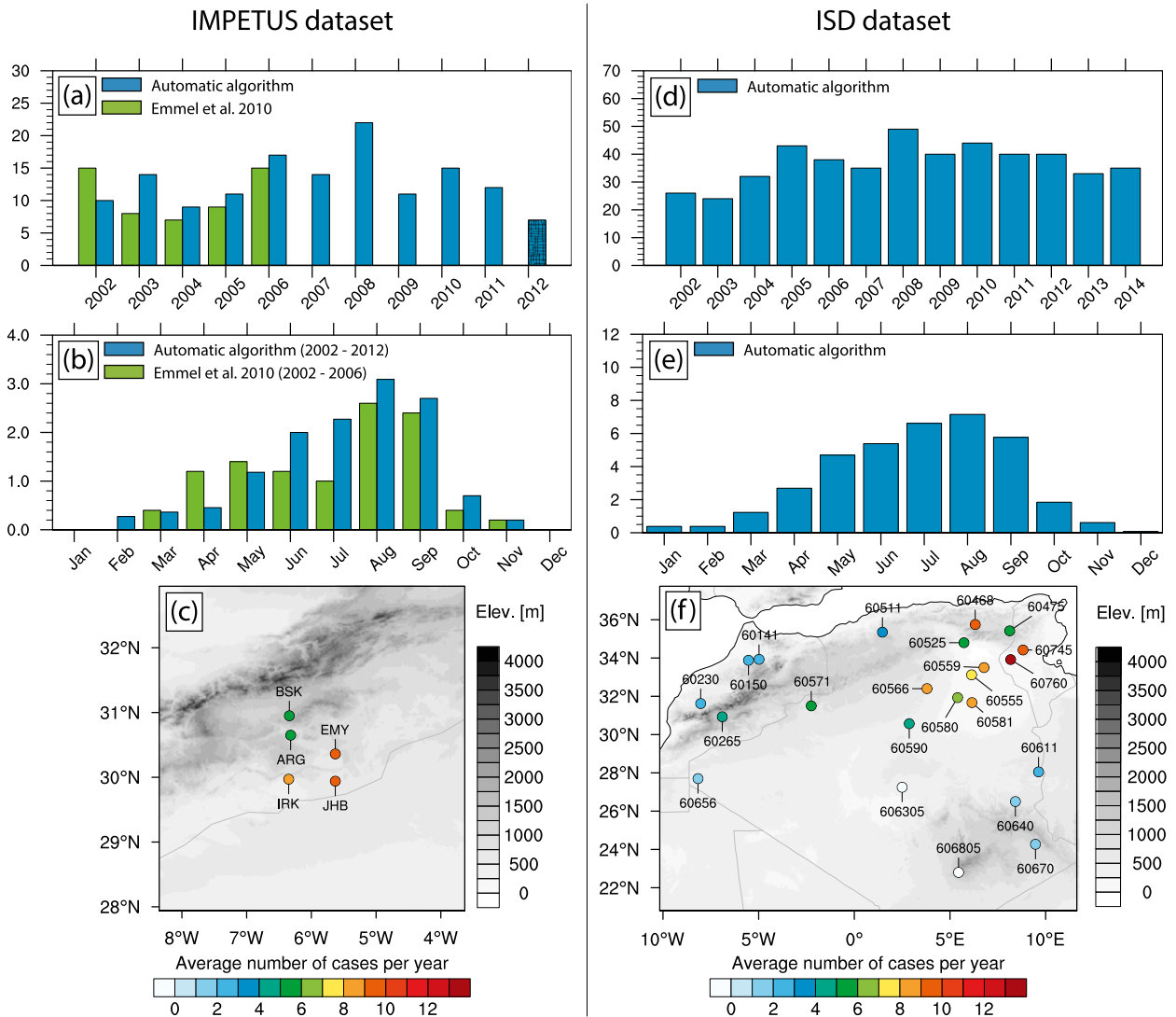
FIG. 5. Climatology of cold pool events created from the (a)–(c) IMPETUS and (d)–(f) ISD datasets: (a),(d) numbers of cases per year; (b),(e) average number of cases per month; and (c),(f) average number of cases per station and year. For all panels only months with more than 80% data availability per station are included in the calculation. The hatching in (a) indicates incomplete data for 2012.

period from 2002 to 2011 shows no clear trend, with an average number of 13.6 cases per year, but with large differences between particular years, ranging from 9 (2004) to 22 (2008) cases per year (Fig. 5a). The year 2012 was very likely the year with the weakest convection activity during the whole period, but the average number of cases per year was calculated without 2012 because of missing data from 23 September onward. Deviations in the numbers of cases per year compared to Emmel et al. (2010) are largest for the years 2002 and 2003. In 2002, Emmel et al. (2010) found five additional cases. One of them did not fulfill the slightly stricter criteria for the station data applied here (T_d has to stay higher for at least 1 h); the other four cases were

identified in station data, but did not fulfill the satellite criteria. Convective systems in these cases were too small or too far away from the stations. However, it is still possible that these cases are also cold pool events, but they were likely to have been weaker than the other events identified by the criteria in the present study. In 2003, the automated algorithm identified six cases more than Emmel et al. (2010), and from 2004 to 2006 two cases more per year. Additional cases are not surprising, because Emmel et al. (2010) used infrared images (10.8 μm) in which high clouds can obscure low-level arc clouds and temperature differences associated with the leading edge of a cold pool. In four of the additional cases from 2003, the microwave images showed multiple

convective cells around the stations. In such a situation contiguous high-level cloud shields are particularly likely. However, it should be remarked here that the automated algorithm is not able to distinguish a synoptic cold front with embedded deep convection from convection not associated with a frontal system.

The annual cycle is unimodal with a maximum in August (Fig. 5b). The average number of cases per month from May to September is 2.3. Emmel et al. (2010) also identified August as the most active month, but found fewer cases for June and July. These differences are also evident for a subsample for the years 2002–06 (not shown) and could be related to midlatitude cyclones and their frontal systems with embedded convection creating ambiguous cases during early summer. Such convection embedded in cloud bands is harder to detect in IR images. The maximum in August coincides with a maximum in midlevel moisture transport from tropical West Africa. These tropical–extratropical interactions (TEI) were analyzed by Knippertz (2003) based on midtropospheric backward trajectories. It could be shown that the majority of the precipitation that fell in August and September at the synoptic station of Ouarzazate (60265), which is in the vicinity of the IMPETUS station network, is related to TEI. In these months, the midlevel moisture transport combined with orographic forcing frequently triggers convection over the Atlas Mountains (Knippertz et al. 2003). The numbers of cases per year and station differ significantly, even between neighboring stations (Fig. 5c), which is likely a consequence of the complex terrain surrounding the stations. This finding is in agreement with Emmel et al. (2010), who also identified EMY and JHB as the stations most often affected by cold pools.

The IMPETUS station network covers only a very small area of the Saharan flank of the Atlas Mountains. With these stations alone, it is difficult to draw conclusions about the whole region and about how representative the IMPETUS stations are for a larger region in North Africa. The ISD dataset described in section 2b helps to overcome this issue. It includes stations with sufficient data availability for Morocco, Algeria, and Tunisia. The larger distances between the stations make it less likely to detect the same cold pool event at more than one station. This is especially relevant for stations without direct neighbors like Bechar (60571) or Tiaret (60511) where the number of detected events per year is reduced by up to 54% as a result of the requirement of a second station. Also, Ouarzazate (60265), which has no direct neighbor on the same side of the High Atlas, is affected with a reduction of 35% or 2.5 events per year. Both the coarser spatial station network and the coarser temporal resolution (30 min to 1 h) of the observations

influence the comparability between the results achieved with both datasets. Nevertheless, the coarser temporal resolution was taken into account by adapted thresholds for ΔT_d (see section 3a). Even if this introduces uncertainty for single cases, averages over longer time periods should be reasonable. An example is Ouarzazate (WMO 60265), which is located close to BSK and ARG. For all three stations the algorithm detects four or five cases per year (Figs. 5c,f). The analyzed time period is too short to calculate a smooth annual cycle from a single station, but as for the IMPETUS stations, the majority of events at Ouarzazate are also detected from May to September (50 of 61 events).

The number of cases per year for the ISD stations is 36.9, with 5.9 cases per month from May to September (Figs. 5d,e). The absolute numbers are larger compared to the IMPETUS stations because of the larger area covered. The pattern of the interannual variability shows similarities in terms of relatively active and inactive years, but also deviations like for 2003, which was relatively inactive using ISD, but not for the IMPETUS stations. Other interesting aspects of the ISD dataset include that 1) the region south of the Saharan Atlas and the Aurès Mountains is more frequently affected by cold pool events than the region south of the High and Anti Atlas (Fig. 5f; see Fig. 1 for geographic names), and consequently, the IMPETUS station network cannot be considered to be representative for the whole south of the Atlas region, and 2) the annual cycle for the IMPETUS stations (Fig. 5b) differs from the annual cycle for the larger region covered by the ISD dataset (Fig. 5e), where the convective activity starts earlier in the year; the number of cold pools observed in May in the ISD station dataset already reaches more than two-thirds of the maximum number in August. May is less active for the IMPETUS stations with about 40% of the August maximum. The retarded increase in the vicinity of the High Atlas is possibly explained by the relocation of the Saharan heat low to the border region between Algeria and Mali. The associated midlevel anticyclonic flow transports moisture along its western side, which has its strongest effect over the High Atlas region (cf. Knippertz et al. 2003; Knippertz 2003). On the contrary, extratropical cyclonic activity might lead to an elevated level of cold pool activity. However, a comprehensive analysis of the regional differences should include moisture transport at different levels, as well as synoptic forcings, which is not within the scope of this study.

b. Satellite-only climatology

It was shown in the last section that the High and Anti Atlas mountain ranges are less often affected by convective cold pool events than regions farther east, but
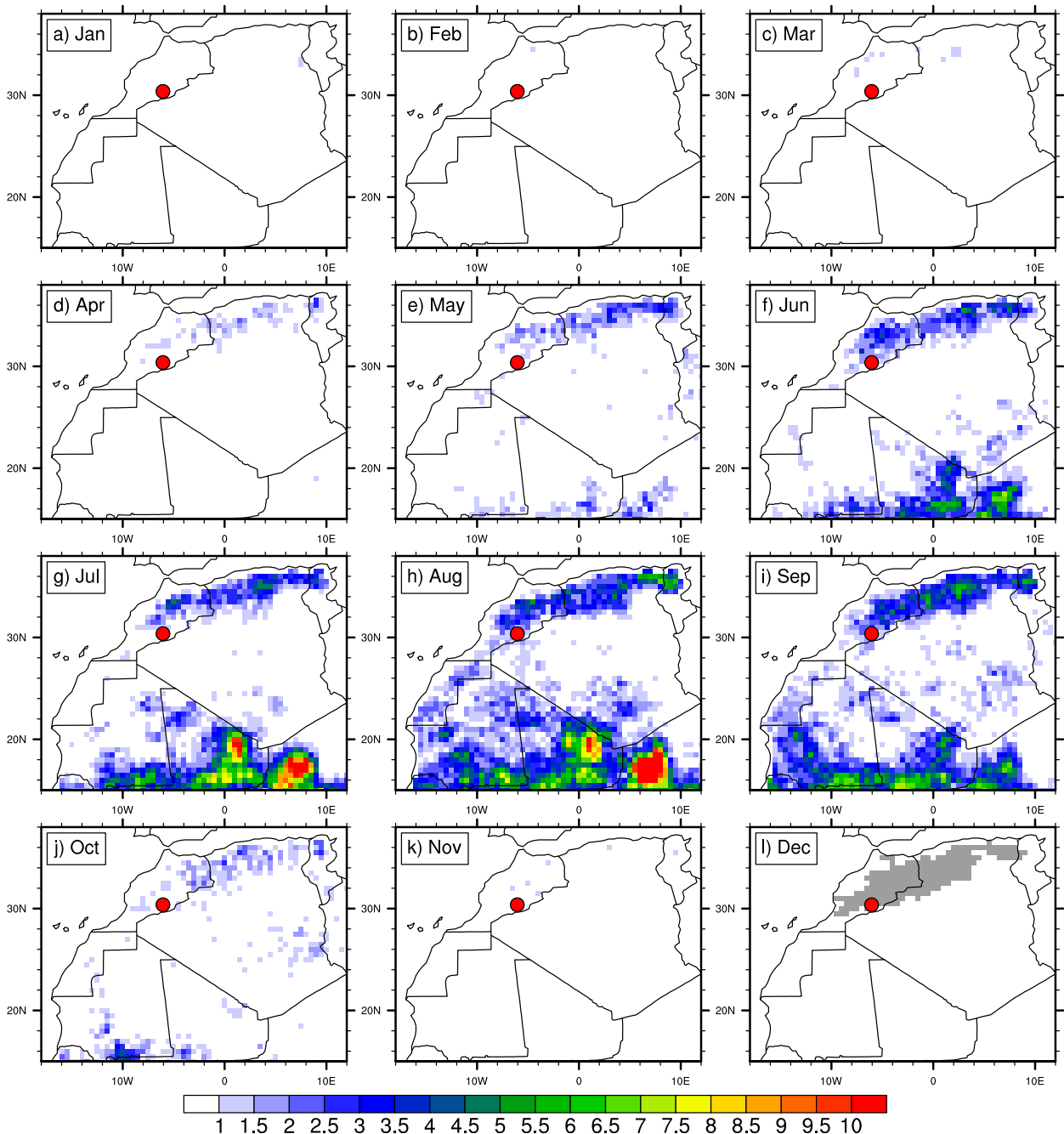
FIG. 6. Annual cycle of convective events in northwest Africa. Shown is the percentage of days when a convective event was detected within one grid cell in the satellite overpass closest to 1800 UTC from 2002 to 2014. The gray color in (l) marks grid points with an elevation of more than 700 m and indicates the area used for the calculation of the AMCI. The red dot indicates the location of the IMPETUS station network.

some uncertainty remains in this statement as the spatial density and the temporal resolution of the station data are relatively low. Therefore, an additional climatology independent of station data was created based on microwave satellite data alone. The climatology covers the region shown in Fig. 6 and was created on a regular

$0.5° \times 0.5°$ grid with data from 2002 to 2014. For each grid cell and each day only the satellite overpass closest to 1800 UTC (maximum in diurnal cycle of convection) was used, which avoids any influences of the varying number of satellites over time, since only one overpass per day was used. For each grid cell the occurrence of

deep convection was counted. If at least one of the satellite pixels within a grid cell fulfilled the threshold criterion (see section 3b), this grid cell was assigned a one; otherwise, a zero was assigned for this day. Finally, long-term monthly means of these counts were calculated. Figure 6 shows their annual evolution. The maximum activity is, consistent with the station datasets, during the West African monsoon months of May–September (Figs. 6e–i). The differences in the spatial distribution of convection between May and June explain the differences between the average number of cases for these months in the ISD and IMPETUS datasets. In May convection over the High Atlas, where the majority of events for the IMPETUS stations originate, is significantly less frequently detected than over the Aurès Mountains where, given the distribution of stations, the majority of the events for the ISD stations originate.

Starting from June, the whole of the Atlas Mountains from Morocco to Tunisia are frequently affected by deep convection, for each grid cell on about 2%–3% of the days. These values are, as one would expect, smaller than in the Sahel region. There, regions with orographic forcing like the Adrar des Ifoghas at the border between Mali and Algeria or the Aïr Massif in northern Niger are affected up to 3 times more often, as is best visible in July and August (Figs. 6g,h).

Despite the agreement in seasonal and geographical behavior between the satellite-only and station climatologies, there seems to be a significant difference in the absolute number of detected threshold exceedances. For the months May–September, the ISD station climatology indicates cold pools generating deep convection on about 20% of the days per months while the values per grid cell in this period are much lower. The reason for this discrepancy is that the satellite-only climatology is by design a climatology of the occurrence of deep convective cells and not of convective cold pool events with large horizontal extent. Figure 2 illustrates that only the cores of convective systems are visible in the microwave image. The example shown is one of the strongest events in the whole period, but only a small number of pixels (10.9%) exceed the threshold for the gradient in brightness temperature. Nevertheless, a comparison with the IMPETUS station data reveals that the occurrence of deep convection can serve as a proxy for cold pool events. For the period 2002–12, 84 events with deep convection were found in a circle of 100-km radius around the IMPETUS stations, 38 of which (45%) were strong enough to fulfill the station criteria.

c. Atlas mountain convection index

Part of the motivation for this study is the question of the frequency of strong convective cold pool events over the Atlas Mountains. This question was addressed here through the introduction of an Atlas mountain convection index (hereafter referred to as AMCI). This index was calculated from all grid cells in the climatology that are located over the Atlas Mountains and whose elevation exceeds 700 m (see Fig. 6l). Virtually all convection in this region occurs in terrain above this level. On a daily basis, the AMCI contains the percentage of grid cells with deep convection and is thus a measure for the size of the convective events over the Atlas Mountains. The time series of this index (Fig. 7) shows the frequent occurrence of deep convection over the Atlas Mountains with a wide range of values. There are many events with small values, most likely weaker, unorganized systems with spatially restricted, smaller cold pools. Long-lived events are created when cold pools from several cells merge and are therefore associated with higher values. To find a meaningful threshold, the IMPETUS station data were considered again. For two-thirds of the cases selected from this dataset by the cold pool detection algorithm, the AMCI values exceed 2.6%. Thus, values above this threshold are assumed to belong to significant cold pool events. As with both station climatologies (Figs. 5a,d), the year-to-year variability of this parameter (Fig. 8a) shows no clear trend over the analyzed time period. The relative changes in the numbers of events detected in consecutive years differ from those found in the station climatologies. This is likely related to the irregular distribution of the stations. The annual cycle of the AMCI (Fig. 8b) shows the same general shape as the annual cycle from the ISD station dataset, but with a slightly larger number of cases per month, which is of course highly dependent on the selected threshold. Another difference is the yearly maximum, which is found in September in AMCI and in August in both station datasets. The maximum activity of convection in September is located over the Tell and the Saharan Atlas Mountains in northern Algeria (Fig. 6i), an area that is not well covered by the station datasets.

In addition to the frequency of occurrence, another interesting aspect of the AMCI time series is the temporal clustering of events. Particularly stronger events (which exceed the 2.6% threshold) seldom occur in isolation. Instead, these events tend to be clustered into multiday episodes. Strong events usually occur on two consecutive days and are embedded into 5-day-long convectively active periods. This finding is in agreement with an analysis of dust episodes in May and June 2006 south of the Atlas Mountains by Knippertz et al. (2009b), which lasted 4–8 days, and the dust events were attributed to synoptic-scale features such as lee cyclones and upper-level troughs. To verify the subjective impression of clustering for the AMCI, a method common in windstorm analysis was applied, the so-called dispersion statistic (Mailier et al. 2006):
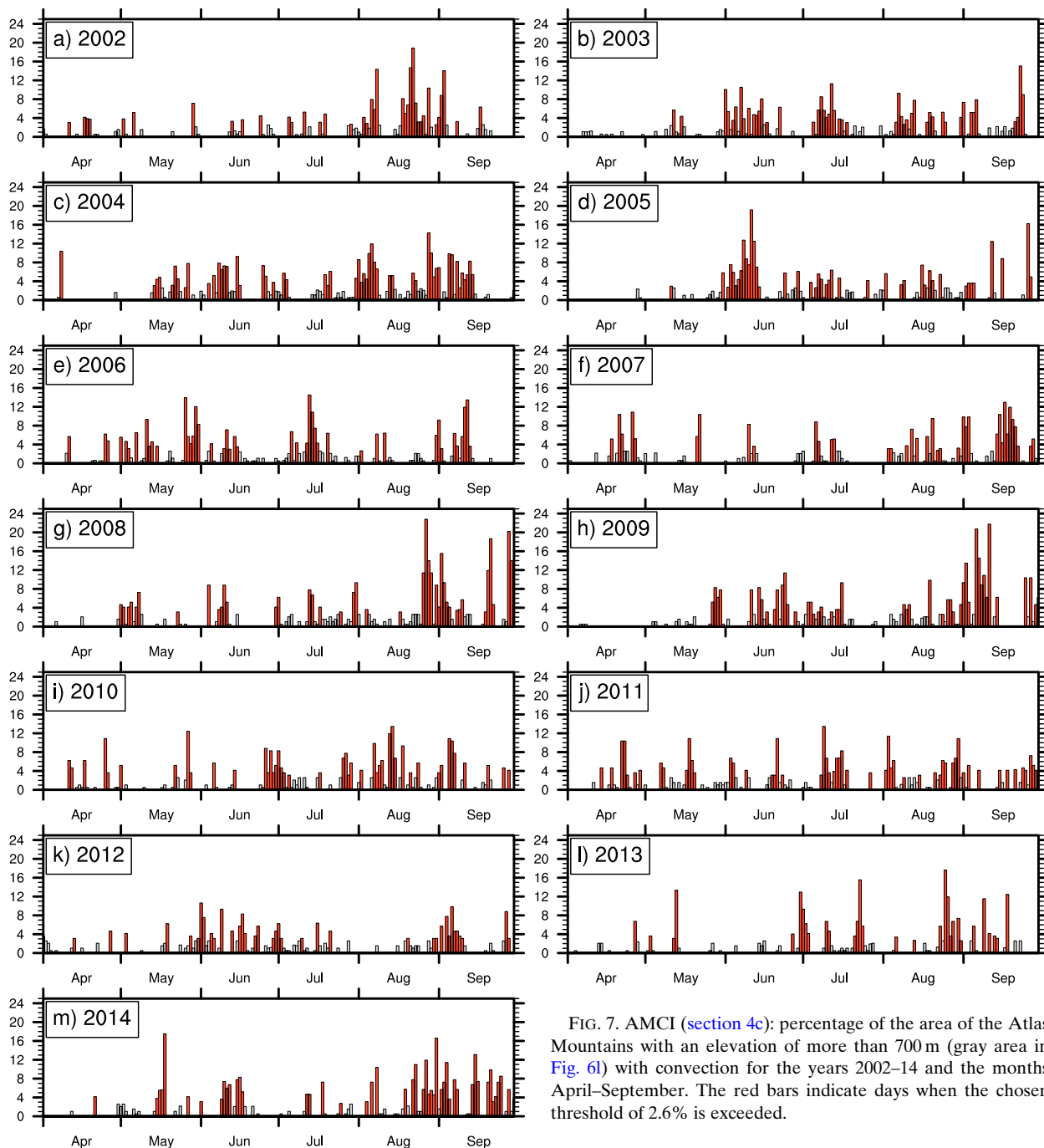
FIG. 7. AMCI (section 4c): percentage of the area of the Atlas Mountains with an elevation of more than 700 m (gray area in Fig. 6l) with convection for the years 2002–14 and the months April–September. The red bars indicate days when the chosen threshold of 2.6% is exceeded.

$$\psi = \text{Var}(n)/E(n) - 1, \qquad (4)$$

where $E(n)$ is the mean and $\text{Var}(n)$ is the variance of n. Equation (4) yields 0 for a homogeneous Poisson process, $\psi > 0$ corresponds to processes that are more clustered than random, and $\psi < 0$ corresponds to processes that are more regular than random. In this case, n is a time series of the number of convective events

(AMCI > 2.6%) in 10-day periods. To avoid the influence of the annual cycle, only the months between June and September were used in the calculation. As expected from visual inspection of Fig. 7, not all years show a statistically significant clustering, but when applied to the whole time series, the dispersion statistic is $\psi = 0.57$, which is statistically significant at the 99.9% level. An answer to the question why some years show a
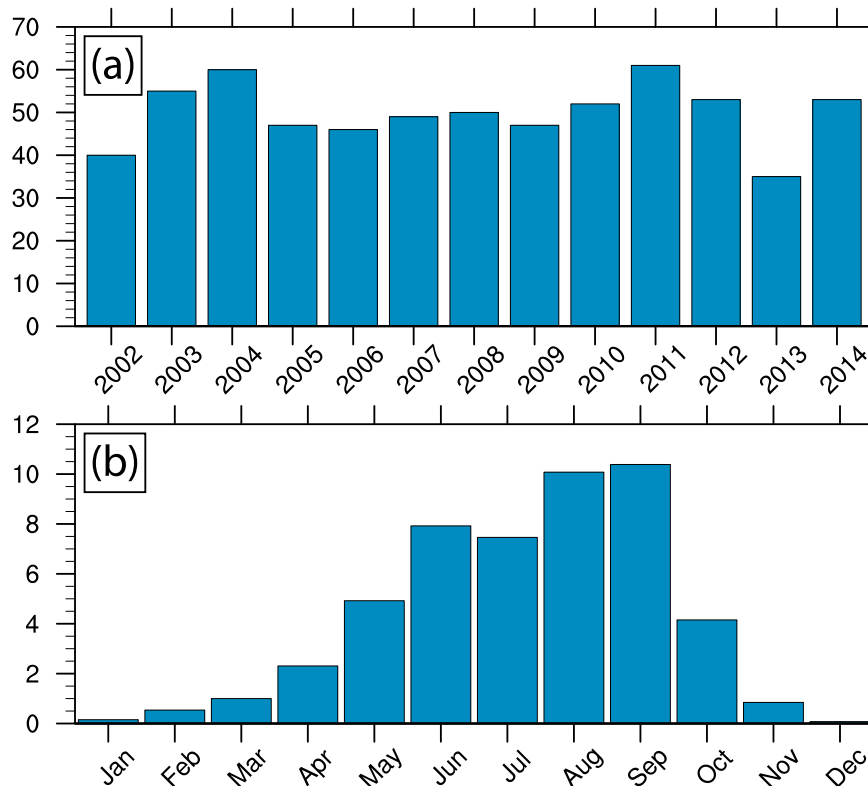
FIG. 8. (a) Number of convective events per year and (b) annual cycle calculated from the AMCI (section 4c) with a threshold of 2.6%.

more pronounced clustering than others would have to include an analysis of synoptic situations. However, this is not within the scope of this study.

5. Summary and discussion

This study has investigated the possibility to create long-term climatologies of convective cold pool events based on routine surface observations and microwave satellite data, both freely available worldwide. The major findings are as follow:

- The presented method is well suited for the objective, automated, and reproducible creation of long-term climatologies of the rather complex quantity of convective cold pool occurrence.
- The method is applicable to surface observations of different temporal resolution. It was shown that comparable results are achievable with automatic weather stations, which offer high temporal resolution, and with WMO standard reports from synoptic stations and airports, which at best offer a temporal resolution of 30 min.
- It was further shown that results obtained only from satellite information are a reasonable proxy for the

occurrence of surface cold pool events in semiarid regions. This is particularly relevant for applications in remote areas like deserts, which lack a dense surface station network. But it should be noted that at least some surface stations are necessary to estimate a relation between convection detected by satellites and the occurrence of cold pools. This relationship may vary from region to region.

- Northwest Africa during the time period from 2002 to 2014 was selected as a showcase for the new method. In the region south of the Atlas Mountains from Morocco to Tunisia the regularity of cold pool events could be demonstrated. For the months May–September, 2.3 (IMPETUS stations) to 5.9 (ISD stations) events were detected. Using satellite information only, it was further shown that convective events in the region of study are not regularly or randomly distributed in time, but tend to cluster into convective periods of 5 days, which often include strong events at two consecutive days.

Applying the developed algorithm to other regions with documented occurrences of haboobs can help to address the open question of the relative importance of these events (Williams 2008; Engelstaedter and

Washington 2008) for total dust emission, especially when the created climatologies are combined with observations of dustiness. Even if the method is designed to be as universal as possible, it is still not effortless to use it in other regions. In addition to the large amount of necessary satellite data to be processed, the criteria for the screening of station data need to be reviewed and potentially adapted. The leading edge of cold pools is always characterized by high wind speed, but its passage is not necessarily accompanied by an increase in dewpoint temperature in wetter environments (Parker et al. 2005). We expect the U.S. desert southwest and Great Plains to be particularly suitable because of the relatively dense METAR station network with hourly or higher-resolved observations. The available Doppler radar network could be used as an additional source of information.

Some sources of uncertainty remain with the presented method. The numbers of cases depend, at least to some extent, on the chosen thresholds for station and satellite data and also on data availability. Instrument failures on the ground, as well as on the satellites, could result in missed cases. Also, false positives are possible in complex synoptic situations where deep convection is embedded in a frontal system. In such cases, the method cannot distinguish between the leading edge of a cold front and a cold pool, as both have characteristics of density currents. However, the created climatologies are a valuable source of information for model evaluation. A direct comparison is possible when a satellite simulator like RTTOV-SCATT (Bauer et al. 2006) or the Atmospheric Radiative Transfer Simulator (ARTS; Buehler et al. 2005a) is applied to the model output. Both present weather and climate models, as well as benefits of new parameterization developments for convective cold pools (e.g., Grandpeix and Lafore 2010; Pantillon et al. 2015), should be assessed by means of long-term observational datasets.

For northwest Africa, the importance of convective cold pools is already emphasized by the regularity of their occurrence but gains additional weight through the clustering in several-days-long periods. Cold pools from Sahel convection form a significant inflow of moisture into the Saharan heat low region (Marsham et al. 2013a) and it is reasonable to assume that the convection at the northern flank also contributes significantly to the Saharan moisture budget. Evan et al. (2015) recently stressed the importance of moisture and its radiative feedback for the deepening of the Saharan heat low in past decades and suggested a connection to the rainfall recovery observed in the Sahel since the 1970s (e.g., Sanogo et al. 2015) and to year-to-year variability of the WAM. In addition to

their effect on the moisture budget and dust emissions, episodes of convective events are also expected to have a direct impact on heat low dynamics through modification of the pressure gradient at the northern flank. We intend to conduct a follow-up study to investigate these larger-scale dynamic effects.

REFERENCES

Allen, C. J. T., R. Washington, and S. Engelstaedter, 2013: Dust emission and transport mechanisms in the central Sahara: Fennec ground-based observations from Bordj Badji Mokhtar, June 2011. *J. Geophys. Res. Atmos.*, **118**, 6212–6232, doi:10.1002/jgrd.50534.

Ashpole, I., and R. Washington, 2013: A new high-resolution central and western Saharan summertime dust source map from automated satellite dust plume tracking. *J. Geophys. Res. Atmos.*, **118**, 6981–6995, doi:10.1002/jgrd.50554.

Atkinson, N. C., 2001: Calibration, monitoring and validation of AMSU-B. *Adv. Space Res.*, **28**, 117–126, doi:10.1016/ S0273-1177(01)00312-X.

Bauer, P., E. Moreau, F. Chevallier, and U. O'Keeffe, 2006: Multiple-scattering microwave radiative transfer for data assimilation applications. *Quart. J. Roy. Meteor. Soc.*, **132**, 1259–1281, doi:10.1256/qj.05.153.

Bennartz, R., and P. Bauer, 2003: Sensitivity of microwave radiances at 85-183 GHz to precipitating ice particles. *Radio Sci.*, **38**, 8075, doi:10.1029/2002RS002626.

Bou Karam, D., E. Williams, M. Janiga, C. Flamant, M. McGraw-Herdeg, J. Cuesta, A. Auby, and C. Thorncroft, 2014: Synoptic-scale dust emissions over the Sahara Desert initiated by a moist convective cold pool in early August 2006. *Quart. J. Roy. Meteor. Soc.*, **140**, 2591–2607, doi:10.1002/qj.2326.

Brindley, H., P. Knippertz, C. Ryder, and I. Ashpole, 2012: A critical evaluation of the ability of the Spinning Enhanced Visible and Infrared Imager (SEVIRI) thermal infrared red-green-blue rendering to identify dust events: Theoretical analysis. *J. Geophys. Res.*, **117**, D07201, doi:10.1029/ 2011JD017326.

Buehler, S. A., P. Eriksson, T. Kuhn, A. von Engeln, and C. Verdes, 2005a: ARTS, the atmospheric radiative transfer simulator. *J. Quant. Spectrosc. Radiat. Transfer*, **91**, 65–93, doi:10.1016/ j.jqsrt.2004.05.051.

——, M. Kuvatov, and V. O. John, 2005b: Scan asymmetries in AMSU-B data. *Geophys. Res. Lett.*, **32**, L24810, doi:10.1029/2005GL024747.

Burns, B., X. Wu, and G. Diak, 1997: Effects of precipitation and cloud ice on brightness temperatures in AMSU moisture channels. *IEEE Trans. Geosci. Remote Sens.*, **35**, 1429–1437, doi:10.1109/36.649797.

Chen, W., and D. W. Fryrear, 2002: Sedimentary characteristics of a haboob dust storm. *Atmos. Res.*, **61**, 75–85, doi:10.1016/S0169-8095(01)00092-8.

Christensen, J., and Coauthors, 2013: Climate phenomena and their relevance for future regional climate change. *Climate Change 2013: The Physical Science Basis*, T. Stocker et al., Eds., Cambridge University Press, 1217–1308.

Cohen, A. E., M. C. Coniglio, S. F. Corfidi, and S. J. Corfidi, 2007: Discrimination of mesoscale convective system environments using sounding observations. *Wea. Forecasting*, **22**, 1045–1062, doi:10.1175/WAF1040.1.

Coniglio, M. C., D. J. Stensrud, and L. J. Wicker, 2006: Effects of upper-level shear on the structure and maintenance of strong quasi-linear mesoscale convective systems. *J. Atmos. Sci.*, **63**, 1231–1252, doi:10.1175/JAS3681.1.

Corfidi, S. F., 2003: Cold pools and MCS propagation: Forecasting the motion of downwind-developing MCSs. *Wea. Forecasting*, **18**, 997–1017, doi:10.1175/1520-0434(2003)018<0997:CPAMPF>2.0.CO;2.

Druyan, L. M., 2011: Studies of 21st-century precipitation trends over West Africa. *Int. J. Climatol.*, **31**, 1415–1424, doi:10.1002/joc.2180.

Emmel, C., P. Knippertz, and O. Schulz, 2010: Climatology of convective density currents in the southern foothills of the Atlas Mountains. *J. Geophys. Res.*, **115**, D11105, doi:10.1029/2009JD012863.

Engelstaedter, S., and R. Washington, 2008: Atmospheric controls on the annual cycle of North African dust. *J. Geophys. Res.*, **113**, D03103, doi:10.1029/2006JD007195.

Engerer, N. A., D. J. Stensrud, and M. C. Coniglio, 2008: Surface characteristics of observed cold pools. *Mon. Wea. Rev.*, **136**, 4839–4849, doi:10.1175/2008MWR2528.1.

Evan, A. T., C. Flamant, S. Fiedler, and O. Doherty, 2014: An analysis of aeolian dust in climate models. *Geophys. Res. Lett.*, **41**, 5996–6001, doi:10.1002/2014GL060545.

——, ——, C. Lavaysse, C. Kocha, and A. Saci, 2015: Water vapor forced greenhouse warming over the Sahara Desert and the recent recovery from the Sahelian drought. *J. Climate*, **28**, 108–123, doi:10.1175/JCLI-D-14-00039.1.

Eymard, L., F. Karbou, S. Janicot, N. Chouaib, and F. Pinsard, 2010: On the use of Advanced Microwave Sounding Unit-A and -B measurements for studying the monsoon variability over West Africa. *J. Geophys. Res.*, **115**, D20115, doi:10.1029/2009JD012935.

Farquharson, J. S., 1937: Haboobs and instability in the sudan. *Quart. J. Roy. Meteor. Soc.*, **63**, 393–414, doi:10.1002/qj.49706327111.

Goff, R. C., 1976: Vertical structure of thunderstorm outflows. *Mon. Wea. Rev.*, **104**, 1429–1440, doi:10.1175/1520-0493(1976)104<1429:VSOTO>2.0.CO;2.

Goldberg, M. D., D. S. Crosby, and L. Zhou, 2001: The limb adjustment of AMSU-A observations: Methodology and validation. *J. Appl. Meteor.*, **40**, 70–83, doi:10.1175/1520-0450(2001)040<0070:TLAOAA>2.0.CO;2.

Grandpeix, J.-Y., and J.-P. Lafore, 2010: A density current parameterization coupled with Emanuel's convection scheme.

Part I: The models. *J. Atmos. Sci.*, **67**, 881–897, doi:10.1175/2009JAS3044.1.

Heinold, B., P. Knippertz, J. H. Marsham, S. Fiedler, N. S. Dixon, K. Schepanski, B. Laurent, and I. Tegen, 2013: The role of deep convection and nocturnal low-level jets for dust emission in summertime West Africa: Estimates from convection-permitting simulations. *J. Geophys. Res. Atmos.*, **118**, 4385–4400, doi:10.1002/jgrd.50402.

Hong, G., 2005: Detection of tropical deep convective clouds from AMSU-B water vapor channels measurements. *J. Geophys. Res.*, **110**, D05205, doi:10.1029/2004JD004949.

Immerkær, J., 1996: Fast noise variance estimation. *Comput. Vision Image Understanding*, **64**, 300–302, doi:10.1006/cviu.1996.0060.

Knippertz, P., 2003: Tropical–extratropical interactions causing precipitation in northwest Africa: Statistical analysis and seasonal variations. *Mon. Wea. Rev.*, **131**, 3069–3076, doi:10.1175/1520-0493(2003)131<3069:TICPIN>2.0.CO;2.

——, and M. C. Todd, 2010: The central west Saharan dust hot spot and its relation to African easterly waves and extratropical disturbances. *J. Geophys. Res.*, **115**, D12117, doi:10.1029/2009JD012819.

——, A. H. Fink, A. Reiner, and P. Speth, 2003: Three late summer/early autumn cases of tropical–extratropical interactions causing precipitation in northwest Africa. *Mon. Wea. Rev.*, **131**, 116–135, doi:10.1175/1520-0493(2003)131<0116:TLSEAC>2.0.CO;2.

——, C. Deutscher, K. Kandler, T. Müller, O. Schulz, and L. Schütz, 2007: Dust mobilization due to density currents in the Atlas region: Observations from the Saharan Mineral Dust Experiment 2006 field campaign. *J. Geophys. Res.*, **112**, D21109, doi:10.1029/2007JD008774.

——, J. Trentmann, and A. Seifert, 2009a: High-resolution simulations of convective cold pools over the northwestern Sahara. *J. Geophys. Res.*, **114**, D08110, doi:10.1029/2008JD011271.

——, and Coauthors, 2009b: Dust mobilization and transport in the northern Sahara during SAMUM 2006—A meteorological overview. *Tellus*, **61B**, 12–31, doi:10.1111/j.1600-0889.2008.00380.x.

Kocha, C., P. Tulet, J. P. Lafore, and C. Flamant, 2013: The importance of the diurnal cycle of aerosol optical depth in West Africa. *Geophys. Res. Lett.*, **40**, 785–790, doi:10.1002/grl.50143.

Labrot, T., L. Lavanant, K. Whyte, N. Atkinson, and P. Brunel, 2011: AAPP documentation: Scientific description. Tech. Rep. NWPSAF-MF-UD-001, Satellite Application Facility for Numerical Weather Prediction, 107 pp. [Available online at https://nwpsaf.eu/deliverables/aapp/NWPSAF-MF-UD-001_Science.pdf.]

Lensky, I. M., and D. Rosenfeld, 2008: Clouds-Aerosols-Precipitation Satellite Analysis Tool (CAPSAT). *Atmos. Chem. Phys.*, **8**, 6739–6753, doi:10.5194/acp-8-6739-2008.

Linden, P. F., and J. E. Simpson, 1985: Microbursts: A hazard for aircraft. *Nature*, **317**, 601–602, doi:10.1038/317601a0.

Mailier, P. J., D. B. Stephenson, C. A. T. Ferro, and K. I. Hodges, 2006: Serial clustering of extratropical cyclones. *Mon. Wea. Rev.*, **134**, 2224–2240, doi:10.1175/MWR3160.1.

Marsham, J. H., D. J. Parker, C. M. Grams, C. M. Taylor, and J. M. Haywood, 2008: Uplift of Saharan dust south of the intertropical discontinuity. *J. Geophys. Res.*, **113**, D21102, doi:10.1029/2008JD009844.

——, N. S. Dixon, L. Garcia-Carreras, G. M. S. Lister, D. J. Parker, P. Knippertz, and C. E. Birch, 2013a: The role of moist convection in the West African monsoon system:

Insights from continental-scale convection-permitting simulations. *Geophys. Res. Lett.*, **40**, 1843–1849, doi:10.1002/grl.50347.

——, and Coauthors, 2013b: Meteorology and dust in the central Sahara: Observations from Fennec supersite-1 during the June 2011 Intensive Observation Period. *J. Geophys. Res. Atmos.*, **118**, 4069–4089, doi:10.1002/jgrd.50211.

Miller, S. D., A. P. Kuciauskas, M. Liu, Q. Ji, J. S. Reid, D. W. Breed, A. L. Walker, and A. A. Mandoos, 2008: Haboob dust storms of the southern Arabian Peninsula. *J. Geophys. Res.*, **113**, D01202, doi:10.1029/2007JD008550.

Offer, Z. Y., and D. Goossens, 2001: Ten years of aeolian dust dynamics in a desert region (Negev desert, Israel): Analysis of airborne dust concentration, dust accumulation and the high-magnitude dust events. *J. Arid Environ.*, **47**, 211–249, doi:10.1006/jare.2000.0706.

Pantillon, F., P. Knippertz, J. Marsham, and C. Birch, 2015: A parameterization of convective dust storms for models with mass-flux convection schemes. *J. Atmos. Sci.*, **72**, 2545–2561, doi:10.1175/JAS-D-14-0341.1.

Parker, D. J., and Coauthors, 2005: The diurnal cycle of the West African monsoon circulation. *Quart. J. Roy. Meteor. Soc.*, **131**, 2839–2860, doi:10.1256/qj.04.52.

Raman, A., A. F. Arellano, and J. J. Brost, 2014: Revisiting haboobs in the southwestern United States: An observational case study of the 5 July 2011 Phoenix dust storm. *Atmos. Environ.*, **89**, 179–188, doi:10.1016/j.atmosenv.2014.02.026.

Rivera Rivera, N. I., T. E. Gill, M. P. Bleiweiss, and J. L. Hand, 2010: Source characteristics of hazardous Chihuahuan Desert dust outbreaks. *Atmos. Environ.*, **44**, 2457–2468, doi:10.1016/j.atmosenv.2010.03.019.

Roberts, A. J., and P. Knippertz, 2014: The formation of a large summertime Saharan dust plume: Convective and synoptic-scale analysis. *J. Geophys. Res. Atmos.*, **119**, 1766–1785, doi:10.1002/2013JD020667.

Sanogo, S., A. H. Fink, J. A. Omotosho, A. Ba, R. Redl, and V. Ermert, 2015: Spatio-temporal characteristics of the recent rainfall recovery in West Africa. *Int. J. Climatol.*, doi:10.1002/joc.4309, in press.

Simpson, J. E., 1987: *Gravity Currents: In the Environment and the Laboratory.* Ellis Horwood Limited, 244 pp.

Smith, A., N. Lott, and R. Vose, 2011: The Integrated Surface Database: Recent developments and partnerships. *Bull. Amer. Meteor. Soc.*, **92**, 704–708, doi:10.1175/2011BAMS3015.1.

Speth, P., M. Christoph, and B. Diekkrüger, Eds., 2010: *Impacts of Global Change on the Hydrological Cycle in West and Northwest Africa.* Springer, 675 pp., doi:10.1007/978-3-642-12957-5.

Strong, C. L., K. Parsons, G. H. McTainsh, and A. Sheehan, 2011: Dust transporting wind systems in the lower Lake Eyre basin, Australia: A preliminary study. *Aeolian Res.*, **2**, 205–214, doi:10.1016/j.aeolia.2010.11.001.

Sutton, L. J., 1925: Haboobs. *Quart. J. Roy. Meteor. Soc.*, **51**, 25–30, doi:10.1002/qj.49705121305.

Takemi, T., 2005: Explicit simulations of convective-scale transport of mineral dust in severe convective weather. *J. Meteor. Soc. Japan*, **83A**, 187–203, doi:10.2151/jmsj.83A.187.

Wark, D. Q., R. H. Brown, D. H. Josephson, and G. W. Withee, 1993: Adjustment of TIROS Operational Vertical Sounder data to a vertical view. NOAA Tech. Rep. NESDIS 64, 36 pp.

Weisman, M. L., and R. Rotunno, 2004: A theory for strong long-lived squall lines revisited. *J. Atmos. Sci.*, **61**, 361–382, doi:10.1175/1520-0469(2004)061<0361:ATFSLS>2.0.CO;2.

Williams, E. R., 2008: Comment on "Atmospheric controls on the annual cycle of North African dust" by S. Engelstaedter and R. Washington. *J. Geophys. Res.*, **113**, D23109, doi:10.1029/2008JD009930.

WMO, 2010: *Part A—Alphanumeric Codes*. Vol. I.1, *Manual on Codes*, WMO-306, World Meteorological Organization, 506 pp.

Xu, X., H. Georg, and S. Zhang, 2009: An algorithm to detect tropical deep convective clouds through AMSU-B water vapor channels. *J. Ocean Univ. China*, **8**, 9–14, doi:10.1007/s11802-009-0009-9.

Xue, Y., and Coauthors, 2010: Intercomparison and analyses of the climatology of the West African monsoon in the West African Monsoon Modeling and Evaluation project (WAMME) first model intercomparison experiment. *Climate Dyn.*, **35**, 3–27, doi:10.1007/s00382-010-0778-2.

Zipser, E. J., 1977: Mesoscale and convective-scale downdrafts as distinct components of squall-line structure. *Mon. Wea. Rev.*, **105**, 1568–1589, doi:10.1175/1520-0493(1977)105<1568:MACDAD>2.0.CO;2.